Geophysical Research Letters

RESEARCH LETTER
10.1029/2018GL081496

Mid-Proterozoic Ferruginous Conditions Reflect Postdepositional Processes

Sarah P. Slotznick[1,2], Samuel M. Webb[3], Joseph L. Kirschvink[1,4], and Woodward W. Fischer[1]

[1]Division of Geological and Planetary Sciences, California Institute of Technology, Pasadena, CA, USA, [2]Now at Earth and Planetary Science, University of California, Berkeley, CA, USA, [3]Stanford Synchrotron Radiation Lightsource, Menlo Park, CA, USA, [4]Earth-Life Science Institute, Tokyo Institute of Technology, Tokyo, Japan

Key Points:
- A pyrrhotite-siderite isograd was identified within the ~1.4-Ga lower Belt group, Belt Supergroup in subgreenschist facies samples
- Diagenetic overprints include recrystallization of iron sulfides, base metal sulfides, nanophase pyrrhotite, and iron-bearing carbonates
- Early diagenetic pyrite and detrital iron oxides suggest the Belt Basin had oxic waters, consistent with cooccurring eukaryotic fossils

Supporting Information:
- Supporting Information S1

Correspondence to:
S. P. Slotznick,
sslotz@berkeley.edu

Citation:
Slotznick, S. P., Webb, S. M., Kirschvink, J. L., & Fischer, W. W. (2019). Mid-Proterozoic ferruginous conditions reflect postdepositional processes. *Geophysical Research Letters*, *46*, 3114–3123. https://doi.org/10.1029/2018GL081496

Received 29 NOV 2018
Accepted 31 JAN 2019
Accepted article online 5 FEB 2019
Published online 18 MAR 2019

Abstract To evaluate the mechanics of mid-Proterozoic environmental iron transport and deposition, we coupled microscale textural and bulk rock magnetic techniques to study the ~1.4-Ga lower Belt group, Belt Supergroup, Montana and Idaho. We identified a pyrrhotite-siderite isograd that marks metamorphic iron-bearing mineral reactions beginning in subgreenschist facies samples. Even in the best-preserved parts of the basin, secondary overprints were common including recrystallization of iron-bearing sulfides, base metal sulfides, and nanophase pyrrhotite. Despite these overprints, a record of redox chemistry was preserved in the early diagenetic framboidal pyrite and detrital iron oxides including trace nanoscale magnetite that remained after sulfidization in anoxic and sulfidic sedimentary pore fluids. Based on these results, we interpret the Belt Basin as having oxic waters, at least in shallow-water environments, with no indication of abundant ferrous iron in the water column; this is consistent with the cooccurrence of early eukaryotic fossils within the same strata.

Plain Language Summary Observing iron chemistry and mineralogy in sedimentary rocks is one of the primary methods for understanding ancient redox environments; today, iron is poorly soluble in seawater due its high dioxygen levels, but some iron-based metrics suggest that ocean and lakes were rich in soluble iron for a billion years after the rise in atmospheric oxygen 2.3 Ga. Using a novel approach for evaluating iron environmental processes, we analyzed the iron-bearing minerals within 1.4-Ga rocks and were able to untangle which minerals were primary, containing information about the ancient environment, and which minerals were secondary, telling the story of later alteration through fluids carrying new elements into the rock or higher temperatures/pressures from burying the sediments. Primary detrital iron minerals implied that the Belt Basin waters were oxygenated, at least in shallow-water environments, contrary to prior work but consistent with the rich fossil record of eukaryotes in the same strata.

1. Introduction

Understanding redox conditions and processes during Proterozoic time is important for understanding the emergence of eukaryotes and complex multicellular life since both depend on O_2 for biosynthesis and metabolic processes (Embley & Martin, 2006; Summons et al., 2006). Iron is the most abundant transition metal at the Earth's surface, and observations of its chemistry and mineralogy in sedimentary rocks have been utilized for decades to understand ancient environmental redox processes as it cycles between +II and +III valence states (e.g., Cloud, 1968). More recently, the bulk sequential extraction technique of iron speciation has dramatically altered views on Proterozoic geochemistry, revealing a complex picture of predominately anoxic iron-rich (i.e., ferruginous) conditions with additional oxic and anoxic H_2S-rich (i.e., euxinic) environments varying in time, geography, and water depth (Poulton & Canfield, 2011; Sperling et al., 2015). However, postdepositional processes especially diagenetic and metamorphic formation of carbonates and iron sulfides can affect iron speciation proxy data (Slotznick, Eiler, & Fischer, 2018). In order to address these issues, we took an approach that is sensitive to the redox state of iron within samples while also preserving textural data to understand how and when the iron-bearing minerals formed—chemical imaging techniques including energy dispersive spectroscopy (EDS) and synchrotron X-ray absorption spectroscopy paired with sensitive bulk rock magnetics. To gain understanding of postdepositional processes, we applied these methods to a location with well-known metamorphic gradients: the mid-Proterozoic Belt Supergroup.

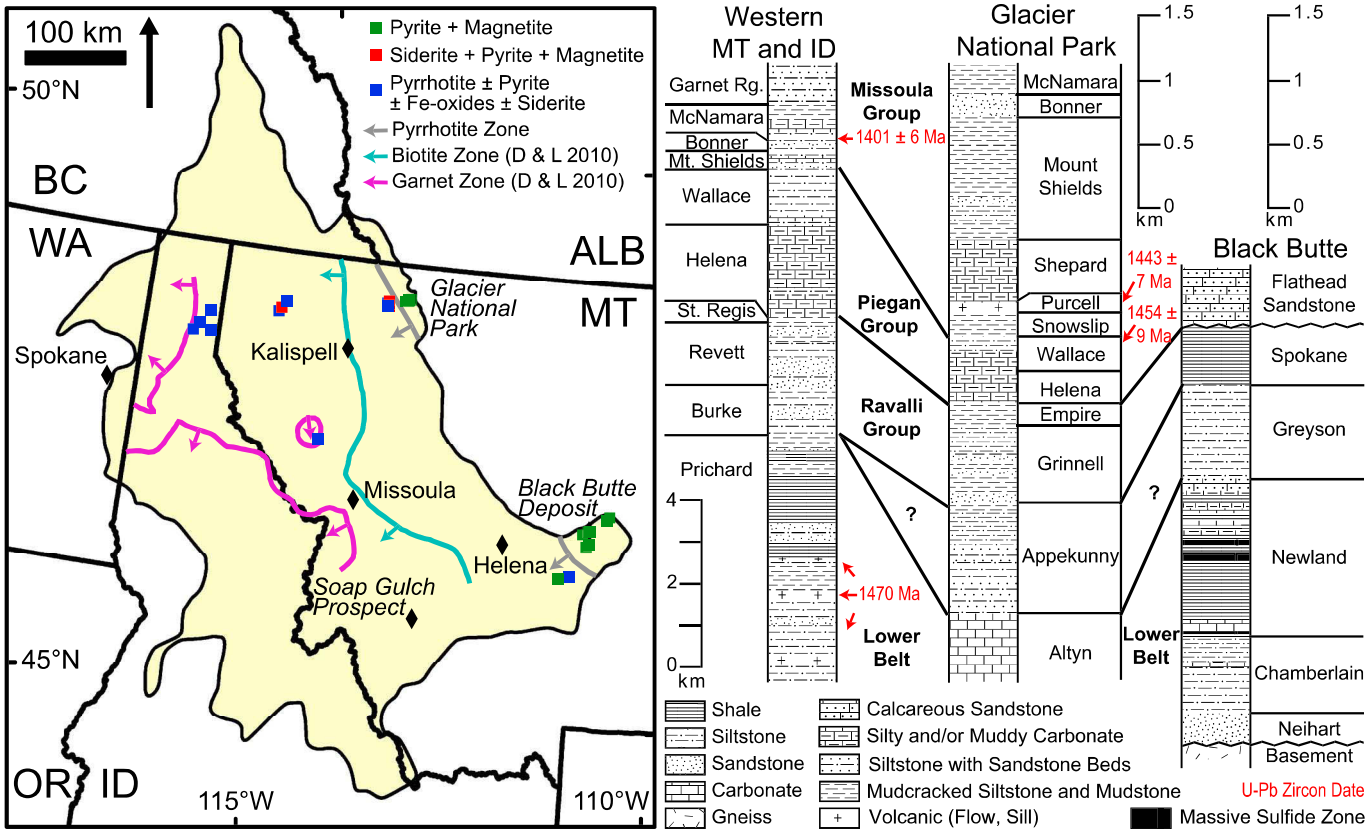

Figure 1. Map showing extent of the Belt Supergroup in the United States and Canada and prior metamorphic zone contours (Duke & Lewis, 2010) with new pyrrhotite-siderite isograd based on samples from the lower Belt group shown with mineralogical color coding highlighting iron mobility during low-grade metamorphism. Stratigraphic nomenclature varies across the sampled formations of the Belt Basin, but they are correlated in broad (in)formally defined groups. Here stratigraphy representing nomenclature for western Montana and northern Idaho (specifically from Plains, Montana) is shown correlated to stratigraphy on the east side of Glacier National Park and stratigraphy near the Black Butte Deposit, the latter representing nomenclature for the entire Helena Embayment (rocks surrounding and east of Helena, Montana). Note the thickening of the sedimentary strata to the west; the western section has a distinct scale bar from the two eastern sections. Stratigraphic data are from Cressman (1989), Slotznick et al. (2015, 2016), Winston (2007), Winston and Link (1993), and U-Pb zircon dates of tuffs, sills, and flows are summarized in Evans et al. (2000).

The Belt Supergroup, dated between 1470 and 1401 Ma (Evans et al., 2000), is an extensive mid-Proterozoic sedimentary succession, exposed across parts of Montana, Idaho, Washington, Alberta, and British Columbia (Figure 1). Over 18 km thick, it contains a mixture of siliciclastic and carbonate rocks (Winston & Link, 1993). The strata also preserve a record of the mid-Proterozoic biosphere with diverse microfossils and macrofossils, some of which are interpreted to be early eukaryotes (e.g., Adam et al., 2017). Regional metamorphic gradients exist due to burial and contact metamorphism, ranging from sub-biotite facies in Glacier National Park and the Helena Embayment to garnet facies by Lake Pend Orielle to staurolite facies near batholiths in Idaho (Duke & Lewis, 2010; Figure 1).

We focused on green, gray, and black shales, siltstones, and sandstones of the lower Belt Supergroup in the United States, which have been previously studied to understand mid-Proterozoic redox conditions. Based on sulfate concentrations, sulfur isotopes, nitrogen isotopes, organic-carbon richness, early diagenetic sulfide-hosted base metal deposits, and basin-wide laminations reminiscent of modern euxinic basins, many previous studies suggested a stratified euxinic basin with oxic surface waters (e.g., Luepke & Lyons, 2001; Lyons et al., 2000; Present et al., 2017; Stüeken, 2013). However, contrary to these proxies, iron speciation results suggested predominantly ferruginous water column conditions with episodic euxinic events (Planavsky et al., 2011). Extracted iron attributed to carbonate salts and magnetite were the main contributors resulting in this ferruginous interpretation. Our study sheds light on this geochemical conclusion,

highlights useful caveats in interpreting iron speciation results, and untangles a complex history of iron mineralization in this basin to arrive at more accurate paleoredox interpretations.

2. Coupled Textural and Bulk Methods

2.1. Belt Supergroup Samples

A total of 63 samples was analyzed from all units of the lower Belt Supergroup (except the carbonate Altyn Formation) and the overlying red and green siliciclastic units of the lower Ravalli Group, spanning a range of metamorphic grades and paleowater depths; photographs, descriptions, and GPS information can be found in Table S1 and Figure S1 in the supporting information and Slotznick et al. (2015, 2016). Within the sub-biotite zone, we controlled for mineralogical variations due to lithologic differences by sampling stratigraphically correlated members of the Appekunny Formation across Glacier National Park (Slotznick et al., 2016) and focusing on the lower Newland Formation across the Helena Embayment.

2.2. Microscale Textural Analyses

When investigating rocks that have undergone diagenesis and metamorphism, it is necessary to observe samples at a microscale to connect chemistry and mineralogy with petrographic textures within the rocks and to ordinate mineralization using crosscutting relationships. First, all samples were made into thin or thick sections and studied using transmitted and reflected optical microscopy. Further petrographic observations were made on select samples in the Caltech GPS Division Analytical Facility using the Zeiss 1550VP field emission scanning electron microscope with a Robinson-type backscatter electron detector for imaging. This instrument contains a paired Oxford X-Max SDD X-ray energy dispersive spectrometer system used to determine X-ray spectra of elemental abundance and HKL electron backscatter diffraction (EBSD) system used to determine structural information. Quantitative chemical information for formula derivation was determined using a JXA-8200 electron probe microanalyzer (EPMA).

In addition to these more conventional textural analyses, we used Caltech's ultrahigh resolution scanning SQuID microscope to create 2-D images of the magnetic field (sensitivity of 0.1 nT) at a resolution of 40–130 μm after giving samples a saturation magnetization in order to identify ferromagnetic minerals texturally. We also performed synchrotron-based X-ray spectroscopy at the Stanford Synchrotron Radiation Lightsource. High-energy X-ray fluorescence (XRF) imaging was performed on thin and thick sections using energies from 20,200 to 10,000 eV at beam line 10-2 to characterize elemental abundances including trace metals over large regions in 30- to 35-μm pixels. Standards for quantification were run at each beam time session with the same collection parameters. Synchrotron-based X-ray absorption near-edge spectroscopy (XANES/XAS) was paired with XRF and elemental imaging using beam lines 14-3 and 2-3 at energies centering around the sulfur absorption edge (2,472 eV) and the iron absorption edge (7,112 eV), respectively. XANES was performed in fluorescence mode at specific 2- to 4-μm-sized spots to determine the chemical form of elements (oxidation state, orbital electronics, type, and number of neighbors). Differences in the shape and K-edge of these absorption spectra can distinguish between a wide range of Fe- and S-bearing minerals (Fleet, 2005; O'Day et al., 2004). Chalcopyrite and pyrrhotite have sufficiently similar S K-edge spectra that high-energy XRF and EDS were applied to confirm the presence of these minerals. Additionally, XRF maps were collected at multiple excitation energies over the XANES spectrum, and images differentiating between phases, coordination environment, and redox state were created by fitting the endmember spectra of different minerals from the sample to the XRF maps (e.g., Mayhew et al., 2011). The six to seven energies chosen for S XRF maps were 2,469.5, 2,470 (not always used), 2,471, 2,472.5, 2,476, 2,482.5, and 2,490 eV and for Fe XRF maps were 7,115, 7,120, 7,122, 7,125, 7,127, and 7,130 eV. At beam line 14-3, the monochromator energy was calibrated by setting the first thiol peak of a sodium thiosulfate powder to 2,472.02 eV. At beam line 2-3, the monochromator energy was calibrated by setting the inflection point of a metallic Fe foil to 7,112 eV. XRF elemental maps were processed using the MicroAnalysis Toolkit (Webb, 2011), and XAS data were processed using SIXPACK (Webb, 2005).

2.3. Rock Magnetic Experiments

On the same sample used for textural analyses and/or on a neighboring specimen, nondestructive bulk rock magnetic experiments were performed to observe fundamental magnetic properties that can distinguish between different magnetic minerals (e.g., Peters & Dekkers, 2003). Rock magnetic experiments were

performed on all samples at the Caltech Paleomagnetics Laboratory using a 2G Enterprises SQuID magnetometer following the RAPID protocols and analyzed using the RAPID Matlab scripts (Kirschvink et al., 2008). Our protocol includes measurements of alternating field demagnetization of the natural remanent magnetization, rotational remanent magnetization acquisition and demagnetization (Potter & Stephenson, 1986; Snowball, 1997; Suzuki et al., 2006; Thomson, 1990), anhysteretic remanent magnetization acquisition and demagnetization, isothermal remanent magnetization (IRM) acquisition and demagnetization (coercivity spectra; Heslop et al., 2002; Robertson & France, 1994), and backfield IRM acquisition. At the Institute for Rock Magnetism at the University of Minnesota, hysteresis loops and direct current demagnetization measurements were also measured on all specimens at room temperature using a Princeton Measurements Vibrating Sample Magnetometer in order to characterize mineralogy (e.g., Roberts et al., 2006; Tauxe et al., 1996), grain size, and magnetite abundance. Using the Quantum Designs Magnetic Property Measurement System at the Institute for Rock Magnetism, select samples were cooled to 10 K under a variety of applied fields to confirm the presence of ferromagnetic minerals using unique low temperature transitions (e.g., Aubourg & Pozzi, 2010; Besnus & Meyer, 1964; Frederichs et al., 2003; Liu et al., 2006; Rochette et al., 1990; Verwey, 1939). Specifically, each sample was cooled in a 2.5-T field from 300 to 10 K, then the field was turned off, and remanence measurements were made upon warming (field-cooled low-temperature saturation IRM). Next, the sample was cooled to 10 K with no applied field, at 10 K it was pulsed with a 2.5 T field, and then remanence measurements were made upon warming (zero-field-cooled low-temperature saturation IRM). Finally, the sample was pulsed with a 2.5-T field at 300 K before cooling to 10 K and warming back to 300 K during which remanence measurements were collected (room temperature saturation IRM).

2.4. Results

Mineralogical results from the lower Belt Supergroup samples are summarized in Figure 1 with additional minerals listed in Table S2. The detailed rock magnetic data, presented in Figures S2–S4, and XANES data (Figure S5) were utilized to make these mineral identifications. Additional identifications were made using EDS, EBSD, and EPMA—examples of these microscale textural analyses including multiple energy XRF maps can be seen in Figures S10–S18.

3. Metamorphic and Diagenetic Overprints

By analyzing correlated strata across known metamorphic gradients, we were able to demarcate a new iron-mineral isograd, as well as note changes to other iron-bearing minerals that occurred through progressive diagenesis/metamorphism. Recognized in both Glacier National Park (Slotznick et al., 2016) and in the Helena Embayment, pyrrhotite and siderite appear only in lower Belt rocks in the western halves of these subbasins (Figure 1). Abundant pyrite, but no pyrrhotite, is present in the lower Belt units to the east of the isograd, suggesting a metamorphic transformation. Pyrrhotite formation can begin at 75–200 °C from the metamorphic transformation of pyrite and either desulfurization or the addition of iron from neighboring iron-bearing minerals or from externally supplied iron-rich fluids (Hall, 1986; Kissin & Scott, 1982). Similarly, siderite identified magnetically using its diagnostic low-temperature transition (Housen et al., 1996) is only found in samples in the western halves of Glacier National Park and the Helena Embayment, while Fe-rich dolomite was identified chemically using EDS and EPMA across these subbasins (Tables S2 and S3). Small, submicron domains of siderite appear to have formed as iron was repartitioned in carbonates or was added from iron silicates, iron sulfides, or iron-rich fluids during burial metamorphism (e.g., French, 1973; Kholodov & Butuzova, 2008). Based on textures and mode of occurrence, we interpret pyrrhotite and siderite as secondary products resulting from burial metamorphism. The pyrrhotite-siderite isograd occurs well below the biotite zone, highlighting that these iron mineral reactions occurred in rocks of very low metamorphic grade (<350 °C, 2.0–2.5 kbar; Duke & Lewis, 2010; Eslinger & Savin, 1973)—in rocks that would not be typically considered “metamorphosed.”

Pyrrhotite and siderite were also observed through the biotite zone/greenschist facies rocks (Duke & Lewis, 2010) further west in the basin. Additional iron mineral transformations were indicated by the appearance of iron calcium aluminosilicates (epidote or pumpellyite) and iron titanium oxides with trace Mn (ilmenite or titanomagnetite; Figure 2c). The textural data suggest metamorphic formation of these phases from Fe-rich dolomite and titanium oxides, respectively, due to their decreased occurrence in western samples (Table S2)

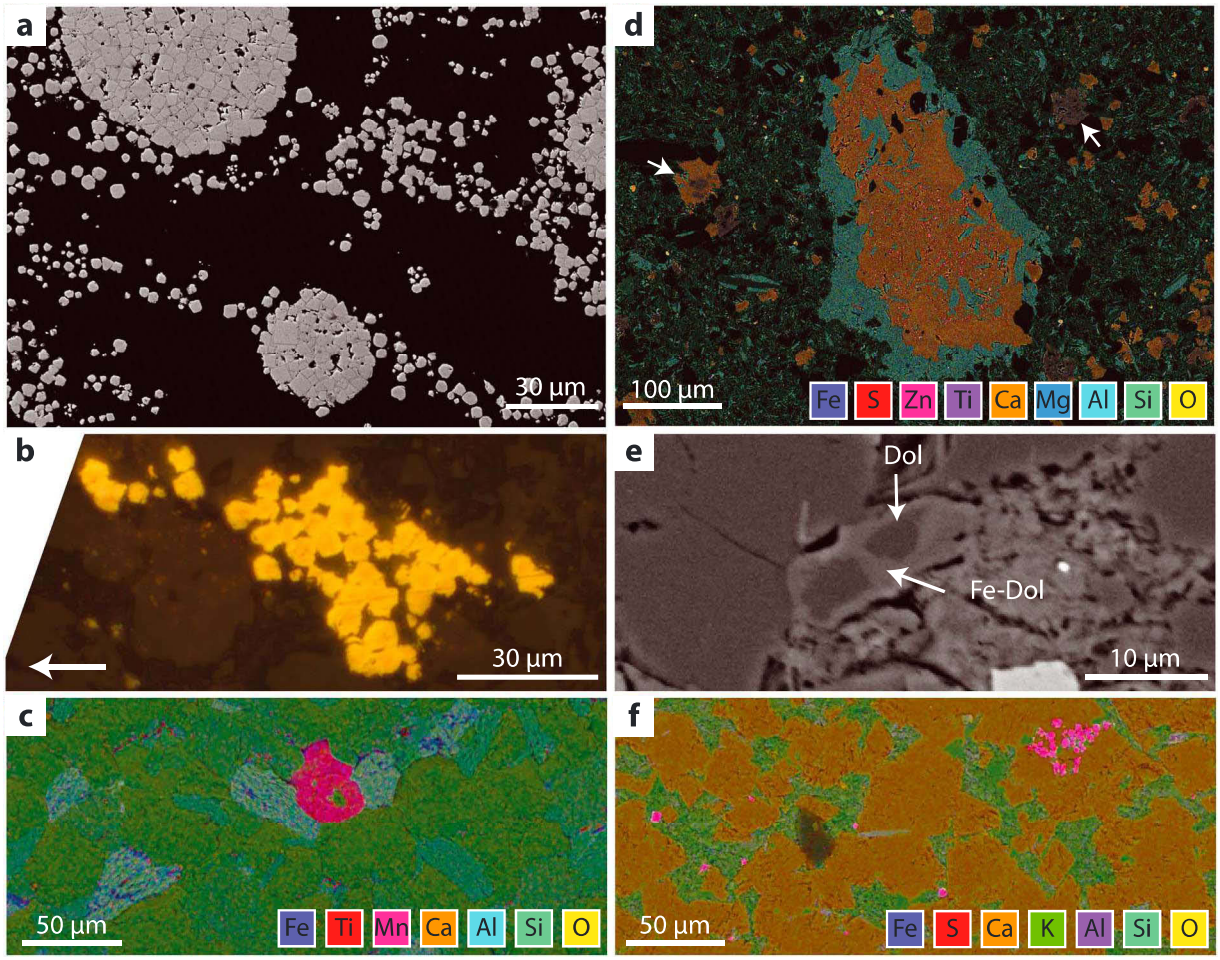

Figure 2. Textural examples from lower Belt samples using backscatter electron imaging, reflected light microscopy, or energy dispersive X-ray spectroscopy overlain on backscatter electron images, all field-oriented unless otherwise stated. (a) Recrystallized framboidal iron sulfides in the Newland Formation (T095-389), (b) pyrite disaggregated framboids from the Appekunny Formation, east Glacier National Park (GP14-35) with arrow pointing in field up-direction, (c) FeTiMnO grain and surrounding coarse-grained matrix from the Prichard Formation (BS13-37), (d) small pyrite grains within calcite nodule rimmed by chlorite with arrows pointing out Fe-dolomite and zoned calcite/Fe-dolomite grains in the Appekunny Formation, west Glacier National Park (GP14-27), (e) dolomite (Dol) rimmed by Fe-bearing dolomite (Fe-Dol) in the Appekunny Formation, east Glacier National Park (GP14-35), and (f) Fe-bearing dolomite cements in the Newland Formation (T112-334).

with additional iron sources including silicates, oxides, sulfides, and/or external fluids (e.g., Bishop, 1972; Ferry, 1988; Muffler & White, 1969). Pyrite recrystallization occurred across the entire Belt Basin, as most of the pyrite occurs in large euhedral grains crosscutting fine-grained sedimentary particles and matrix minerals (e.g., Figures S12 and S17). However, there is a notable increase in grain size to the west, seen in both the matrix minerals and in the iron oxides and sulfides (from <50 µm to >1 mm, compare Figures S10–S12 to S13–S15 to S16–S18). Rock magnetic analyses also revealed the recrystallization of magnetite into other ferromagnetic minerals with increasing metamorphism (Figure S2), highlighting the mobility of iron in greenschist facies rocks.

Quantitative analysis of synchrotron XRF maps highlighted similar amounts of iron and base metals across the basin (Table S4 and Figures S6–S9); this is consistent with the redistribution of metals by the pervasive diagenetic basinal brines identified in previous studies (González-Álvarez & Kerrich, 2010; González-Álvarez et al., 2006). Even in the sub-biotite zone, electron and X-ray spectroscopy identified common Cu, Pb, Zn, and Ag sulfide-bearing minerals (Figures S10–S18). Multiple sulfide phases often occur within the same sedimentary nodule emphasizing that recrystallization of pyrite incorporated trace metals. Chlorite and calcite rims observed around base-metal-bearing pyrrhotite and pyrite nodules on the west side of Glacier National Park (Figures 2d and 3) highlight additional redox reactions that moved iron from

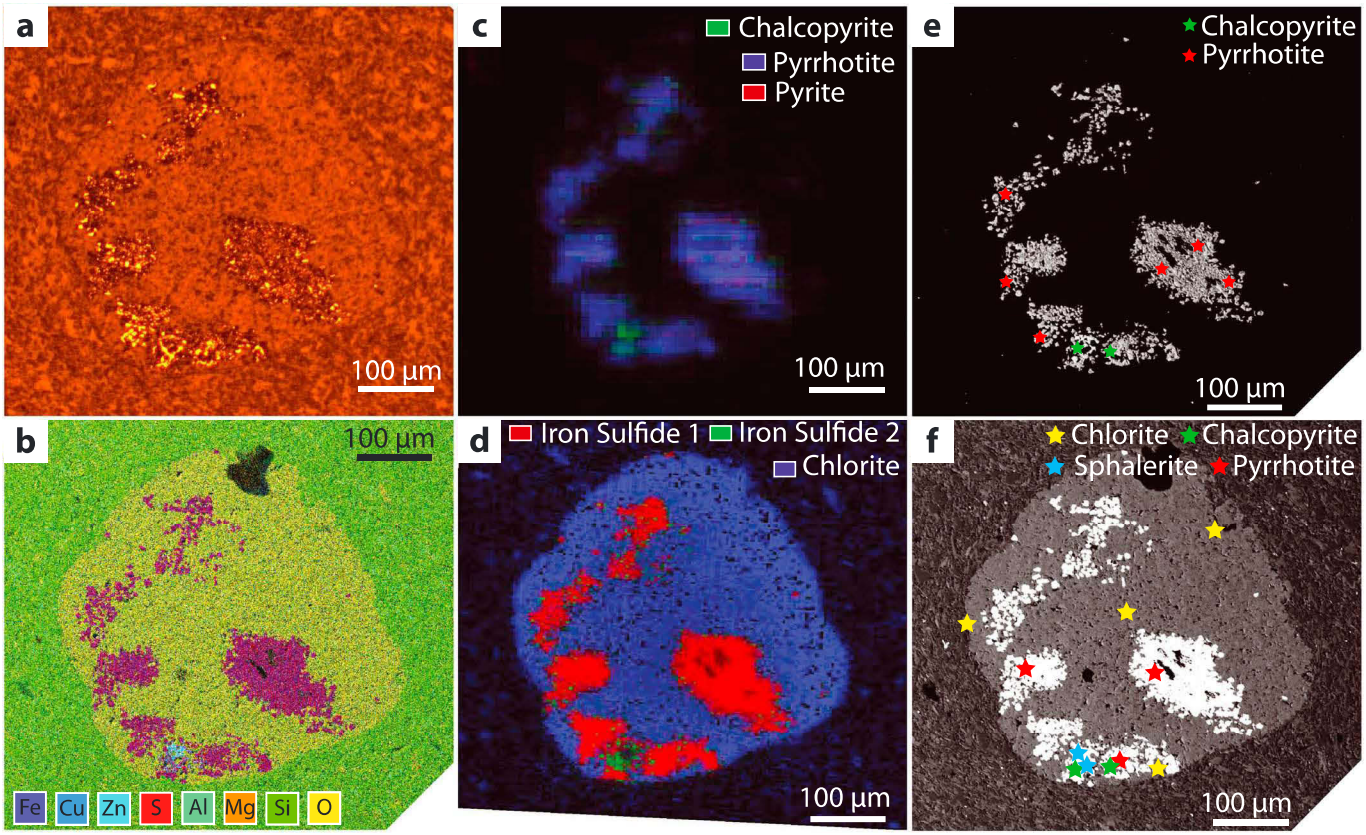

Figure 3. Textural analysis of sample GP12-8, west side of Glacier National Park revealing a metamorphic pyrrhotite recrystallized nodule with chalcopyrite and sphalerite inclusions and later chlorite replacing part of the original nodule. (a) Reflected light microscopy, (b) energy dispersive X-ray spectroscopy, (c) multiple energy X-ray fluorescence maps fit using X-ray absorption near-edge spectra (Figure S13) at sulfur energies and (d) at iron energies, (e) electron backscatter diffraction point mineral identifications on backscatter electron image (patterns in Figure S13), and (f) electron probe microanalyzer point mineral identifications on backscatter electron image (exact formulas in Table S3).

sulfides to silicates and carbonates. To the east of the pyrrhotite-siderite isograd, rock magnetic experiments identified nanophase pyrrhotite (i.e., pyrrhotite below the micron-size-threshold for ferromagnetism) in almost all lower Belt samples (Figure 4a) suggesting metamorphic pyrrhotite formation had begun in small domains within pyrite. The movement of iron from pyrite to other phases—or out of the system entirely—will affect iron speciation data and complicate interpretations of paleoredox (Slotznick, Eiler, & Fischer, 2018).

We observed substantial amounts of Fe-bearing dolomite within the Helena Embayment and Glacier National Park in addition to the siderite in western samples, and textures indicated that these phases are space-filling cements or secondary diagenetic transformations with zonation related to burial diagenesis (Figures 2d–2f). Therefore, we interpreted the Fe-bearing carbonates in the best-preserved lower Belt samples as indicative of a suite of postdepositional processes—there are no textural observations that indicate the formation and transport of these phases in the water column. Their presence skews iron speciation results toward incorrectly implying ferruginous conditions (Slotznick, Eiler, & Fischer, 2018).

4. Primary Mineralogy and Paleoredox Processes

With an appreciation for the substantial suite of processes that altered iron mineralogy after deposition in the Belt Basin, we focused on the least-metamorphosed and least-altered samples to elucidate the primary mineralogy and paleoredox conditions during deposition. Pyrite is present in almost all of the sampled lower Belt rocks, although it is often recrystallized with its petrogenesis uncertain. However, in the best-preserved rocks of the lower Belt group, there are small aggregates of euhedral pyrite grains similar to the pyrite

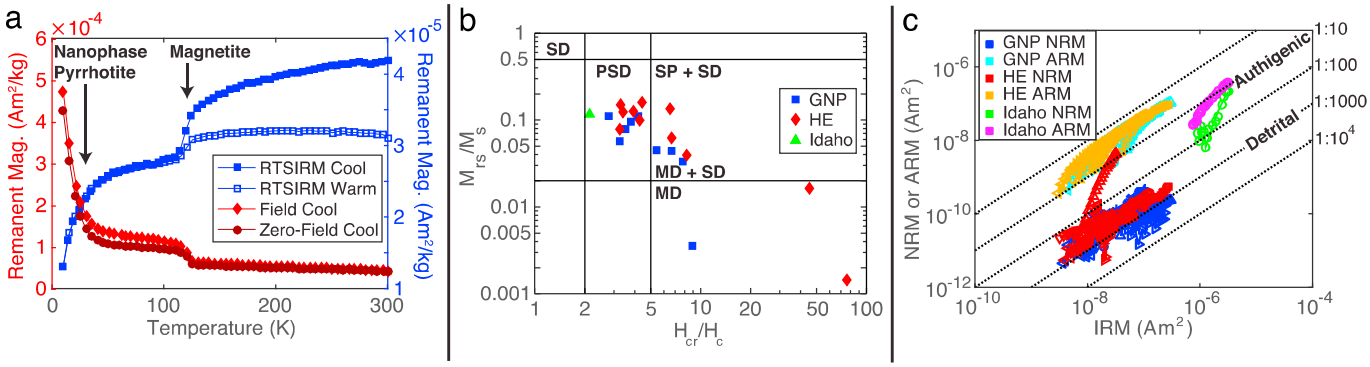

Figure 4. Rock magnetic measurements on samples where magnetite is the predominant ferromagnetic mineral. (a) Measurements after room temperature saturation magnetization (RTSIRM) during cooling and warming as well as measurements upon warming of low temperature saturation magnetization after either cooling in a field or cooling in zero field on a sample from the east side of Glacier National Park (GP12-1) identify magnetite and suggest the presence of nanophase pyrrhotite (also Figures S3b and S3e). (b) Day Plot for grain size implies that most of the magnetite is pseudo-single-domain (PSD, 0.1 to 20 μm; Day et al., 1977; Dunlop, 2002). (c) Fuller test for nature of magnetization distinguishes whether the natural remanent magnetization (NRM) is a weak detrital magnetization or a stronger authigenic chemical magnetization based on comparison to experimental magnetizations and empirical calibrations (Fuller et al., 2002); it highlights that most of the magnetite is detrital in the GNP and HE regions whereas a metamorphosed, garnet zone sample from Idaho as well as one from the Black Butte Deposit have authigenic magnetite. Mag. = magnetization; SD = single-domain; MD = multidomain; SP = superparamagnetic; M_{rs} = remanent saturation magnetization; M_s = saturation magnetization; H_{cr} = coercivity of remanent magnetization; H_c = coercivity; GNP = glacier National Park; HE = Helena embayment; IRM = isothermal remanent magnetization; ARM = anhysteretic remanent magnetization.

framboids known to grow in modern organic-rich sediments (Figures 2a and 2b). Further, based on modern surveys and hydrodynamic calculations of suspension and settling (Wilkin et al., 1996), their large size implies these pyrite textures formed in sedimentary pore fluids. Other macroscopic and microscopic textures such as differential compaction, pyritic debris flow clasts, and detrital pyrite tube structures emphasize the early timing of pyrite mineralization (Figure S19; Present et al., 2017).

One of the most interesting results was the ubiquity of magnetite in all samples from the lower Belt (other than the red Appekunny Member 1) based on rock magnetic analyses (Figures 4 and S2–S4). In many samples from the east side of the Glacier National Park and Helena Embayment regions, magnetite is the only ferromagnetic mineral present other than minor goethite from surface weathering (Table S2, exceptions include massive sulfide zones and red strata). A Day Plot of the magnetite-bearing samples indicated that the magnetite grain size is typically between 0.1 and 20 μm (pseudo-single-domain; Day et al., 1977; Dunlop, 2002; Figure 4b). The Fuller test results indicated that the magnetite in these regions is detrital in origin (Fuller et al., 2002; Figure 4c). Magnetite abundance, calculated by comparing the mass-normalized saturation magnetization with that of pure magnetite (Klein et al., 2014), in all lower Belt samples is approximately 1–8 ppm (Table S5); this is much lower than the 0.08 to 0.7 wt% magnetite inferred from the iron speciation extraction for magnetite in samples from the same formation (Planavsky et al., 2011; see supporting information; Algoe et al., 2012; Burton et al., 2006; Raiswell et al., 2011; Reinhard et al., 2009; Reuschel et al., 2012; Slotznick, Swanson-Hysell, & Sperling, 2018). We therefore interpret the magnetite as detrital grains that remained after incomplete reaction with porewater sulfide to form pyrite. Directly overlying the lower Belt strata, the Grinnell Formation and the Spokane Formation are large deposits of shallow-water hematite-rich siltstone and shale; Appekunny Member 1 within the lower Belt also contains strata rich in ferric phases. Paleomagnetic field tests indicate that these phases are syn-depositional (Elston et al., 2002) and highlight the oxic nature of shallow-water environments in the Belt Basin. Based on our analyses, detrital magnetite also served as an important flux of highly reactive iron to the basin; its preservation suggests water column and pore fluid chemistry was not rich enough in either H_2S to scavenge all of the highly reactive iron to form pyrite or ferrous iron to recrystallize the detrital magnetite to chemically precipitate authigenic magnetite (Canfield & Berner, 1987; Skomurski et al., 2010) although protection of the magnetite by armoring could aid in preservation as well (Chang et al., 2016). Early diagenetic pyrite framboids and Fe-dolomite diagenetic cements in the lower Belt samples highlight the presence of anoxic and sulfidic pore fluid conditions; these euxinic conditions potentially extended into deep portions of the water column in downdip settings in the Helena Embayment and further to the west.

5. Implications for the Biosphere

Our detailed microscale textural and bulk magnetic case study of the mid-Proterozoic Belt Supergroup highlights the value of chemical imaging and rock magnetic techniques to peel away metamorphic and diagenetic alteration to assess primary mineralogy and paleoredox processes. The oxygenated waters suggested by our results would have been able to support the early eukaryotic biosphere fossilized in the same strata (Adam et al., 2016; Adam et al., 2017). Almost all eukaryotes today contain mitochondria, and comparative biology of extant groups suggests that this was also true of their last common eukaryotic ancestor (Embley & Martin, 2006). Mitochondrial electron transport chains are anchored in a very high-potential version of aerobic respiration by A-family heme-copper O_2 reductases (Wikstrom et al., 2015). This mitochondrial aerobic respiration pathway is at home in oxic environments (>0.01 present atmospheric O_2 levels; Fenchel & Finlay, 1995).

Although it is expected that ferrous iron would dominate the compositions of seawater in the absence of life (Walker & Brimblecombe, 1985), upon the rise of atmospheric O_2 ~2.3 Ga, riverine input of detrital iron oxides and sulfate would have increased substantially as seen in the Belt Supergroup (this study; Present et al., 2017). Due to sulfate reduction outpacing iron delivery, all large modern anoxic basins are also sulfidic, for example, the Black Sea and Cariaco Basin (Lyons & Severmann, 2006). Our study suggests iron delivery and dissolution chemistry in the Belt Basin was very similar to water bodies today and deep waters could have become anoxic and euxinic, but there is no indication of abundant ferrous iron in the water column. The often complex petrogenesis of carbonates, a common mineral in the fine-grained rocks typically targeted for iron speciation, means iron-bearing carbonates do not necessarily indicate a ferruginous water column. If the processes responsible for iron mineralization in the Belt Basin are common to sedimentary basins, then it might be valuable to reexamine specific data sets throughout Earth history to test ferruginous redox interpretations and revisit hypotheses that invoke dominant ferruginous conditions during mid-Proterozoic time.

Acknowledgments
We thank D. Winston, G. Zieg, M. Jackson, C. Roach, T. Lyons, A. Chadwick, and 2013 Agouron Field Course members for assistance during sample collection and analysis. We thank J. Grotzinger, A. Sessions, and N. Swanson-Hysell for insightful comments on earlier drafts of this manuscript as well as three anonymous reviewers. Data supporting the conclusions of this paper can be found in the supporting information. Samples from Glacier National Park were collected under NPS Collection Permits GLAC-2012-SCI-0195 and GLAC-2014-SCI-0008. Support for this work was provided by the Agouron Institute, the Tobacco Root Geological Society, the Belt Association, a GSA Student Research Grant, NASA Exobiology, the Packard Foundation, NSF Graduate Research Fellowship, NASA Earth and Space Science Fellowship, and a PEO Scholar Award. Portions of this research were carried out at the Stanford Synchrotron Radiation Lightsource, SLAC National Accelerator Laboratory, a DOE Office of Science User Facility, and as a U.S. Visiting Student Fellow at the Institute for Rock Magnetism at the University of Minnesota, a National Multi-user Facility supported by NSF and the University of Minnesota.

References

Adam, Z. R., Skidmore, M. L., & Mogk, D. W. (2016). Paleoenvironmental implications of an expanded microfossil assemblage from the Chamberlain Formation. *Geological Society of America Special Papers*, *522*, 101–119. https://doi.org/10.1130/2016.2522(04)

Adam, Z. R., Skidmore, M. L., Mogk, D. W., & Butterfield, N. J. (2017). A Laurentian record of the earliest fossil eukaryotes. *Geology*, *45*(5), 387–390. https://doi.org/10.1130/G38749.1

Algoe, C., Stoops, G., Vandenberghe, R., & Van Ranst, E. (2012). Selective dissolution of Fe–Ti oxides—Extractable iron as a criterion for andic properties revisited. *Catena*, *92*, 49–54. https://doi.org/10.1016/j.catena.2011.11.016

Aubourg, C., & Pozzi, J.-P. (2010). Toward a new <250 °C pyrrhotite–magnetite geothermometer for claystones. *Earth and Planetary Science Letters*, *294*(1-2), 47–57. https://doi.org/10.1016/j.epsl.2010.02.045

Besnus, M., & Meyer, A. (1964). Nouvelles données expérimentales sur le magnétisme de la pyrrhotine naturelle, paper presented at Proc. Int. Conf. Mag., Nottingham.

Bishop, D. (1972). Progressive metamorphism from prehnite-pumpellyite to greenschist facies in the Dansey Pass area, Otago, New Zealand. *Geological Society of America Bulletin*, *83*(11), 3177–3198.

Burton, E. D., Bush, R. T., & Sullivan, L. A. (2006). Sedimentary iron geochemistry in acidic waterways associated with coastal lowland acid sulfate soils. *Geochimica et Cosmochimica Acta*, *70*(22), 5455–5468. https://doi.org/10.1016/j.gca.2006.08.016

Canfield, D. E., & Berner, R. A. (1987). Dissolution and pyritization of magnetite in anoxie marine sediments. *Geochimica et Cosmochimica Acta*, *51*(3), 645–659. https://doi.org/10.1016/0016-7037(87)90076-7

Chang, L., Roberts, A. P., Heslop, D., Hayashida, A., Li, J., Zhao, X., et al. (2016). Widespread occurrence of silicate-hosted magnetic mineral inclusions in marine sediments and their contribution to paleomagnetic recording. *Journal of Geophysical Research: Solid Earth*, *121*, 8415–8431. https://doi.org/10.1002/2016JB013109

Cloud, P. E. (1968). Atmospheric and hydrospheric evolution on the primitive earth. *Science*, *160*(3829), 729–736. https://doi.org/10.1126/science.160.3829.729

Cressman, E. R. (1989). *Reconnaissance stratigraphy of the Prichard Formation (Middle Proterozoic) and the early development of the Belt Basin*, *Professional Paper* (Vol. 1490, p. 80). Washington, Idaho, and Montana: United States Geological Survey.

Day, R., Fuller, M., & Schmidt, V. (1977). Hysteresis properties of titanomagnetites: Grain-size and compositional dependence. *Physics of the Earth and Planetary Interiors*, *13*(4), 260–267.

Duke, E. F., & Lewis, R. S. (2010). Near infrared spectra of white mica in the Belt Supergroup and implications for metamorphism. *American Mineralogist*, *95*(7), 908–920.

Dunlop, D. J. (2002). Theory and application of the Day plot (Mrs/Ms versus Hcr/Hc) 1. Theoretical curves and tests using titanomagnetite data. *Journal of Geophysical Research*, *107*(B3), 2057. https://doi.org/10.1029/2001JB000487

Elston, D., Enkin, R., Baker, J., & Kisilevsky, D. (2002). Tightening the belt: Paleomagnetic-stratigraphic constraints on deposition, correlation, and deformation of the Middle Proterozoic (ca. 1.4 Ga) Belt-Purcell Supergroup, United States and Canada. *Geological Society of America Bulletin*, *114*(5), 619–638.

Embley, T. M., & Martin, W. (2006). Eukaryotic evolution, changes and challenges. *Nature*, *440*(7084), 623–630. https://doi.org/10.1038/nature04546

Eslinger, E. V., & Savin, S. M. (1973). Oxygen isotope geothermometry of the burial metamorphic rocks of the Precambrian Belt Supergroup, Glacier National Park, Montana. *Geological Society of America Bulletin*, *84*(8), 2549–2560.

Evans, K. V., Aleinikoff, J. N., Obradovich, J. D., & Fanning, C. M. (2000). SHRIMP U-Pb geochronology of volcanic rocks, Belt Supergroup, western Montana: Evidence for rapid deposition of sedimentary strata. *Canadian Journal of Earth Sciences*, *37*(9), 1287–1300.

Fenchel, T., & Finlay, B. J. (1995). *Ecology and evolution in anoxic worlds*. Oxford; New York: Oxford University Press.

Ferry, J. M. (1988). Infiltration-driven metamorphism in northern New England, USA. *Journal of Petrology*, *29*(6), 1121–1159.

Fleet, M. E. (2005). XANES spectroscopy of sulfur in earth materials. *The Canadian Mineralogist*, *43*(6), 1811–1838. https://doi.org/10.2113/gscanmin.43.6.1811

Frederichs, T., Von Dobeneck, T., Bleil, U., & Dekkers, M. (2003). Towards the identification of siderite, rhodochrosite, and vivianite in sediments by their low-temperature magnetic properties. *Physics and Chemistry of the Earth, Parts A/B/C*, *28*(16–19), 669–679. https://doi.org/10.1016/S1474-7065(03)00121-9

French, B. M. (1973). Mineral assemblages in diagenetic and low-grade metamorphic iron-formation. *Economic Geology*, *68*(7), 1063–1074. https://doi.org/10.2113/gsecongeo.68.7.1063

Fuller, M., Kidane, T., & Ali, J. (2002). AF demagnetization characteristics of NRM, compared with anhysteretic and saturation isothermal remanence: An aid in the interpretation of NRM. *Physics and Chemistry of the Earth, Parts A/B/C*, *27*(25–31), 1169–1177. https://doi.org/10.1016/s1474-7065(02)00127-4

González-Álvarez, I., & Kerrich, R. (2010). REE and HFSE mobility due to protracted flow of basinal brines in the Mesoproterozoic Belt-Purcell Supergroup, Laurentia. *Precambrian Research*, *177*(3-4), 291–307. https://doi.org/10.1016/j.precamres.2009.12.008

González-Álvarez, I., Kusiak, M. A., & Kerrich, R. (2006). A trace element and chemical Th–U total Pb dating study in the lower Belt-Purcell Supergroup, Western North America: Provenance and diagenetic implications. *Chemical Geology*, *230*(1-2), 140–160. https://doi.org/10.1016/j.chemgeo.2005.12.004

Hall, A. J. (1986). Pyrite-pyrrhotine redox reactions in nature. *Mineralogical Magazine*, *50*(356), 223–229. https://doi.org/10.1180/minmag.1986.050.356.05

Heslop, D., Dekkers, M., Kruiver, P., & Van Oorschot, I. (2002). Analysis of isothermal remanent magnetization acquisition curves using the expectation-maximization algorithm. *Geophysical Journal International*, *148*(1), 58–64.

Housen, B. A., Banerjee, S., & Moskowitz, B. (1996). Low-temperature magnetic properties of siderite and magnetite in marine sediments. *Geophysical Research Letter*, *23*(20), 2843–2846.

Kholodov, V., & Butuzova, G. Y. (2008). Siderite formation and evolution of sedimentary iron ore deposition in the Earth's history. *Geology of Ore Deposits*, *50*(4), 299–319. https://doi.org/10.1134/S107570150804003X

Kirschvink, J. L., Kopp, R. E., Raub, T. D., Baumgartner, C. T., & Holt, J. W. (2008). Rapid, precise, and high-sensitivity acquisition of paleomagnetic and rock-magnetic data: Development of a low-noise automatic sample changing system for superconducting rock magnetometers. *Geochemistry, Geophysics, Geosystems*, *9*, Q05Y01. https://doi.org/10.1029/2007GC001856

Kissin, S., & Scott, S. (1982). Phase relations involving pyrrhotite below 350 degrees C. *Economic Geology*, *77*(7), 1739–1754. https://doi.org/10.2113/gsecongeo.77.7.1739

Klein, F., Bach, W., Humphris, S. E., Kahl, W.-A., Jöns, N., Moskowitz, B., & Berquó, T. S. (2014). Magnetite in seafloor serpentinite—Some like it hot. *Geology*, *42*(2), 135–138. https://doi.org/10.1130/G35068.1

Liu, Q., Yu, Y., Torrent, J., Roberts, A. P., Pan, Y., & Zhu, R. (2006). Characteristic low-temperature magnetic properties of aluminous goethite [α-(Fe, Al) OOH] explained. *Journal of Geophysical Research*, *111*, B12S34. https://doi.org/10.1029/2006JB004560

Luepke, J. J., & Lyons, T. W. (2001). Pre-Rodinian (Mesoproterozoic) supercontinental rifting along the western margin of Laurentia: Geochemical evidence from the Belt-Purcell Supergroup. *Precambrian Research*, *111*(1), 79–90. https://doi.org/10.1016/S0301-9268(01)00157-7

Lyons, T. W., Luepke, J. J., Schreiber, M. E., & Zieg, G. A. (2000). Sulfur geochemical constraints on Mesoproterozoic restricted marine deposition: Lower Belt Supergroup, northwestern United States. *Geochimica et Cosmochimica Acta*, *64*(3), 427–437. https://doi.org/10.1016/S0016-7037(99)00323-3

Lyons, T. W., & Severmann, S. (2006). A critical look at iron paleoredox proxies: New insights from modern euxinic marine basins. *Geochimica et Cosmochimica Acta*, *70*(23), 5698–5722. https://doi.org/10.1016/j.gca.2006.08.021

Mayhew, L., Webb, S., & Templeton, A. (2011). Microscale imaging and identification of Fe speciation and distribution during fluid–mineral reactions under highly reducing conditions. *Environmental Science & Technology*, *45*(10), 4468–4474. https://doi.org/10.1021/es104292n

Muffler, L. P., & White, D. E. (1969). Active metamorphism of upper Cenozoic sediments in the Salton Sea geothermal field and the Salton Trough, southeastern California. *Geological Society of America Bulletin*, *80*(2), 157–182.

O'Day, P. A., Rivera, N., Root, R., & Carroll, S. A. (2004). X-ray absorption spectroscopic study of Fe reference compounds for the analysis of natural sediments. *American Mineralogist*, *89*(4), 572–585.

Peters, C., & Dekkers, M. (2003). Selected room temperature magnetic parameters as a function of mineralogy, concentration and grain size. *Physics and Chemistry of the Earth, Parts A/B/C*, *28*(16), 659–667.

Planavsky, N. J., McGoldrick, P., Scott, C. T., Li, C., Reinhard, C. T., Kelly, A. E., et al. (2011). Widespread iron-rich conditions in the mid-Proterozoic Ocean. *Nature*, *477*(7365), 448–451. https://doi.org/10.1038/nature10327

Potter, D., & Stephenson, A. (1986). The detection of fine particles of magnetite using anhysteretic and rotational remanent magnetizations. *Geophysical Journal International*, *87*(2), 569–582.

Poulton, S. W., & Canfield, D. E. (2011). Ferruginous conditions: A dominant feature of the ocean through Earth's history. *Elements*, *7*(2), 107–112. https://doi.org/10.2113/gselements.7.2.107

Present, T. M., Bergmann, K. D., Myers, C., Slotznick, S. P., Creveling, J. R., Zieg, J., et al. (2017). Pyrite-walled tube structures in a Mesoproterozoic sediment-hosted metal sulfide deposit. *GSA Bulletin*, *130*(3-4), 598–616.

Raiswell, R., Reinhard, C. T., Derkowski, A., Owens, J., Bottrell, S. H., Anbar, A. D., & Lyons, T. W. (2011). Formation of syngenetic and early diagenetic iron minerals in the late Archean Mt. McRae Shale, Hamersley Basin, Australia: New insights on the patterns, controls and paleoenvironmental implications of authigenic mineral formation. *Geochimica et Cosmochimica Acta*, *75*(4), 1072–1087. https://doi.org/10.1016/j.gca.2010.11.013

Reinhard, C. T., Raiswell, R., Scott, C., Anbar, A. D., & Lyons, T. W. (2009). A late Archean sulfidic sea stimulated by early oxidative weathering of the continents. *Science*, *326*(5953), 713–716. https://doi.org/10.1126/science.1176711

Reuschel, M., Melezhik, V., & Strauss, H. (2012). Sulfur isotopic trends and iron speciation from the c. 2.0 Ga Pilgujärvi Sedimentary Formation, NW Russia. *Precambrian Research*, *196*, 193–203.

Roberts, A. P., Liu, Q., Rowan, C. J., Chang, L., Carvallo, C., Torrent, J., & Horng, C. S. (2006). Characterization of hematite (α-Fe_2O_3), goethite (α-FeOOH), greigite (Fe_3S_4), and pyrrhotite (Fe_7S_8) using first-order reversal curve diagrams. *Geophysical Journal International*, *111*, B12S35. https://doi.org/10.1029/2006JB004715

Robertson, D., & France, D. (1994). Discrimination of remanence-carrying minerals in mixtures, using isothermal remanent magnetisation acquisition curves. *Physics of the Earth and Planetary Interiors*, *82*(3), 223–234.

Rochette, P., Fillion, G., Mattéi, J.-L., & Dekkers, M. J. (1990). Magnetic transition at 30–34 kelvin in pyrrhotite: Insight into a widespread occurrence of this mineral in rocks. *Earth and Planetary Science Letters*, *98*(3-4), 319–328. https://doi.org/10.1016/0012-821X(90)90034-U

Skomurski, F. N., Kerisit, S., & Rosso, K. M. (2010). Structure, charge distribution, and electron hopping dynamics in magnetite (Fe_3O_4) (100) surfaces from first principles. *Geochimica et Cosmochimica Acta*, *74*(15), 4234–4248. https://doi.org/10.1016/j.gca.2010.04.063

Slotznick, S. P., Eiler, J. M., & Fischer, W. W. (2018). The effects of metamorphism on iron mineralogy and the iron speciation redox proxy. *Geochimica et Cosmochimica Acta*, *224*, 96–115. https://doi.org/10.1016/j.gca.2017.12.003

Slotznick, S. P., Swanson-Hysell, N. L., & Sperling, E. A. (2018). Oxygenated Mesoproterozoic lake revealed through magnetic mineralogy. *Proceedings of the National Academy of Sciences of the United States of America*, *115*(51), 12,938–12,943. https://doi.org/10.1073/pnas.1813493115

Slotznick, S. P., Winston, D., Webb, S. M., Kirschvink, J. L., & Fischer, W. W. (2016). Iron mineralogy and redox conditions during deposition of the Mid-Proterozoic Appekunny Formation, Belt Supergroup, Glacier National Park. *Geological Society of America Special Papers*, *522*, 221–242. https://doi.org/10.1130/2016.2522(09)

Slotznick, S. P., Zieg, J., Webb, S. M., Kirschvink, J. L., & Fischer, W. W. (2015). Iron mineralogy and redox chemistry of the Mesoproterozoic Newland Formation in the Helena Embayment, Belt Supergroup, Montana. *Northwest Geology*, *44*, 55–72.

Snowball, I. F. (1997). The detection of single-domain greigite (Fe3S4) using rotational remanent magnetization (RRM) and the effective gyro field (Bg): Mineral magnetic and palaeomagnetic applications. *Geophysical Journal International*, *130*(3), 704–716.

Sperling, E. A., Wolock, C. J., Morgan, A. S., Gill, B. C., Kunzmann, M., Halverson, G. P., Macdonald, F. A., et al. (2015). Statistical analysis of iron geochemical data suggests limited late Proterozoic oxygenation. *Nature*, *523*(7561), 451–454. https://doi.org/10.1038/nature14589

Stüeken, E. E. (2013). A test of the nitrogen-limitation hypothesis for retarded eukaryote radiation: Nitrogen isotopes across a Mesoproterozoic basinal profile. *Geochimica et Cosmochimica Acta*, *120*, 121–139. https://doi.org/10.1016/j.gca.2013.06.002

Summons, R. E., Bradley, A. S., Jahnke, L. L., & Waldbauer, J. R. (2006). Steroids, triterpenoids and molecular oxygen. *Philosophical Transactions of the Royal Society, B: Biological Sciences*, *361*(1470), 951–968. https://doi.org/10.1098/rstb.2006.1837

Suzuki, Y., Kopp, R. E., Kogure, T., Suga, A., Takai, K., Tsuchida, S., et al. (2006). Sclerite formation in the hydrothermal-vent "scaly-foot" gastropod—Possible control of iron sulfide biomineralization by the animal. *Earth and Planetary Science Letters*, *242*(1-2), 39–50. https://doi.org/10.1016/j.epsl.2005.11.029

Tauxe, L., Mullender, T., & Pick, T. (1996). Potbellies, wasp-waists, and superparamagnetism in magnetic hysteresis. *Journal of Geophysical Research*, *101*(B1), 571–583. https://doi.org/10.1029/95JB03041

Thomson, G. F. (1990). The anomalous demagnetization of pyrrhotite. *Geophysical Journal International*, *103*(2), 425–430.

Verwey, E. (1939). Electronic conduction of magnetite (Fe_3O_4) and its transition point at low temperatures. *Nature*, *144*(3642), 327–328. https://doi.org/10.1038/144327b0

Walker, J. C., & Brimblecombe, P. (1985). Iron and sulfur in the pre-biologic ocean. *Precambrian Research*, *28*(3–4), 205–222. https://doi.org/10.1016/0301-9268(85)90031-2

Webb, S. M. (2005). SIXPACK: A graphical user interface to XAS analysis using IFEFFIT. *Physica Scripta*, *T115*, 1011–1014.

Webb, S. M. (2011). The MicroAnalysis Toolkit: X-ray fluorescence image processing software, AIP Conference Proceedings, 1365, 196–199.

Wikstrom, M., Sharma, V., Kaila, V. R., Hosler, J. P., & Hummer, G. (2015). New perspectives on proton pumping in cellular respiration. *Chemical Reviews*, *115*(5), 2196–2221. https://doi.org/10.1021/cr500448t

Wilkin, R., Barnes, H., & Brantley, S. (1996). The size distribution of framboidal pyrite in modern sediments: An indicator of redox conditions. *Geochimica et Cosmochimica Acta*, *60*(20), 3897–3912. https://doi.org/10.1016/0016-7037(96)00209-8

Winston, D. (2007). Revised stratigraphy and depositional history of the Helena and Wallace Formations, Mid-Proterozoic Piegan Group, Belt Supergroup Montana and Idaho. In P. K. Link & R. S. Lewis (Eds.), *Proterozoic Geology of Western North America and Siberia: Society for Sedimentary Geology (SEPM) Special Publication* (Vol. 86, pp. 65–100).

Winston, D., & Link, P. (1993). Middle Proterozoic rocks of Montana, Idaho and eastern Washington: the Belt Supergroup. In J. Reed, P. Simms, R. Houston, D. Rankin, P. Link, R. Van Schmus, et al. (Eds.), *Precambrian: Conterminous US: The Geology of North America* (Vol. 2, pp. 487–517).